

# 1 Triple collocation validates CONUS-wide evapotranspiration inferred from 2 atmospheric conditions

3

4 Erica L. McCormick<sup>1,\*</sup>, Lillian E. Sanders<sup>1,2</sup>, Kaighin A. McColl<sup>3,4</sup>, Alexandra G. Konings<sup>1</sup>

5

6 <sup>1</sup> Department of Earth System Science, Stanford University

7 <sup>2</sup> Department of Computer Science, Stanford University

8 <sup>3</sup> Department of Earth and Planetary Sciences, Harvard University

9 <sup>4</sup> School of Engineering and Applied Sciences, Harvard University

10 \*Corresponding author: ericamcc@stanford.edu

## 11 **Abstract**

12 Large-scale estimation of evapotranspiration (ET) remains challenging because no  
13 direct remote sensing estimates of ET exist and because most data-driven estimation  
14 approaches require assumptions about the impact of moisture conditions and  
15 biogeography on ET. The surface flux equilibrium (SFE) approach offers an alternative,  
16 deriving ET directly from atmospheric temperature and humidity under the assumption  
17 that conditions in the atmospheric boundary layer reflect ET's land boundary condition.  
18 We present a 4 km resolution, continental United States-wide, daily ET dataset spanning  
19 from 1979 to 2025 using the SFE method. The Bowen ratio is first calculated using the  
20 SFE method solely based on temperature and specific humidity estimates from gridMET  
21 and then converted to ET using net radiation and ground heat fluxes from ERA5-Land.  
22 We evaluate its performance using extended triple collocation to estimate the standard  
23 deviation of the random error and the correlation coefficient of SFE ET compared to true  
24 ET, as well as those of three widely used alternative ET datasets: GLEAM, FluxCom,  
25 and ERA5-Land. Despite its extreme simplicity, SFE ET achieves performance  
26 comparable to or exceeding the other datasets across large portions of CONUS,  
27 particularly in the Western U.S., while requiring no information about land surface,  
28 vegetation, or soil properties and no assumptions about ET's response to environmental  
29 and climate drivers. Our results support the use of SFE as a scalable,  
30 observation-driven method for estimating ET.

31

## 32 **1. Introduction**

33 Evapotranspiration (ET) dominates the terrestrial water cycle (Friedlingstein et al., 2019;  
34 Good et al., 2015), controls the partitioning of radiation into latent and sensible heat  
35 (McColl and Rigden, 2020), and plays a key role in driving the hydrologic cycle by

36 returning water to the atmosphere (Oki and Kanae, 2006). ET therefore has  
37 downstream feedbacks on temperature (Teuling et al., 2010), precipitation, and  
38 vegetation productivity (Green et al., 2017) in addition to directly impacting the carbon  
39 cycles through the trade-off between photosynthesis and transpiration (Yang et al.,  
40 2023). However, estimation of ET via remote sensing remains a significant challenge  
41 with implications for understanding of vegetation response to drought, fire risk, and the  
42 accounting of freshwater resources.

43 One challenge for ET remote sensing is that, unlike some surface properties  
44 such as temperature, we are unable to directly sense the flux of water or latent heat  
45 associated with ET electromagnetically. Therefore, ET products must leverage  
46 modelling approaches - either physical, hybrid, or machine learning - constrained by the  
47 data that is observable via remote sensing. These modelling approaches for ET often  
48 assume - implicitly or explicitly - the response of evaporation and transpiration to  
49 environmental drivers, such as drought or variations in land cover.

50 Alternatively, surface flux equilibrium (SFE) is a data-driven method for  
51 estimating ET directly from atmospheric conditions without relying on soil or vegetation  
52 parameterization. The concept of surface flux equilibrium was first proposed by McColl  
53 et al. (2019) and states that, under many circumstances, the atmosphere and land  
54 surface are coupled so that changes in surface fluxes (including ET) are reflected in  
55 atmospheric temperature and humidity. This approach has several advantages over  
56 other ET estimation methods. It requires no information about vegetation, soil, or  
57 subsurface properties. It also makes no assumptions about root-zone moisture status or  
58 vegetation response to water availability. This means it is well suited for hydrological  
59 research attempting to interrogate the relationship between ET and water availability or  
60 between ET and vegetation cover (or other biogeographic drivers). Additionally, SFE  
61 includes no tunable parameters and can be computed easily using only three inputs - air  
62 temperature, humidity, and net radiation - each of which is readily available at global  
63 scales (McColl and Rigden, 2020).

64 However, more complex ET estimation methods would be expected to  
65 outperform SFE in many settings due to its extreme simplicity and lack of adjustable  
66 parameters. Nevertheless, previous SFE implementation and validation efforts indicate  
67 that SFE performance is comparable - or even better than - other ET estimation  
68 methods at the point- and watershed- scale (Chen et al., 2021; McColl and Rigden,  
69 2020; Thakur et al., 2025). For example, SFE ET has been found to be within the range  
70 of in situ measurement uncertainty at a selection of inland eddy covariance towers, an  
71 upper limit on the performance of any ET estimate (McColl and Rigden, 2020). Thakur  
72 et al. (2025) also calculated SFE ET at inland eddy covariance sites across the  
73 continental United States (CONUS) using tower-based temperature, humidity, and net  
74 radiation. They found that SFE ET outperformed remotely sensed ET from MODIS (Mu

75 et al., 2011) as well as from three ET algorithms using data from the ECOsystem  
76 Spaceborne Thermal Radiometer Experiment on Space Station (ECOSTRESS): the  
77 Simplified Surface Energy Balance (Savoca et al., 2013) SSEBop, (Savoca et al.,  
78 2013), the atmosphere-land exchange inverse disaggregation algorithm (DisALEXI) and  
79 the Priestley-Taylor Jet Propulsion Laboratory model (PT-JPL, Fisher et al., 2020).

80 Thakur et al. (2025) further investigated the impact of input data on SFE  
81 performance by calculating SFE ET using three scenarios: only eddy covariance data,  
82 by using the North American Land Data Assimilation System (NLDAS, Xia et al., 2012)  
83 for temperature and humidity and the Clouds and the Earth's Radiant Energy System  
84 instrument (CERES, Doelling et al., 2013) for net radiation, and by finally using NLDAS  
85 for temperature and humidity and MODIS for net radiation. All three SFE ET  
86 implementations compared favorably to tower-based ET with R2 of 0.70, 0.68, and 0.67  
87 for the tower-based SFE, CERES-based SFE, and MODIS-based SFE, respectively.  
88 This suggests that the emergent simplicity of ET that SFE takes advantage of is robust  
89 to choices of input data, at least at the scale of eddy covariance towers.

90 The only gridded estimates of SFE ET are reported by Chen et al. (2021), who  
91 calculated monthly ET at 0.125o across CONUS using net radiation from CERES and  
92 2-m temperature and humidity from North American Regional Reanalysis (NARR,  
93 Mesinger et al., 2006). They compared SFE ET to estimates from the Coupled Model  
94 Intercomparison Project phase 6 (CMIP6, Eyring et al., 2016) and to water  
95 balance-based ET estimates available at large catchments across CONUS. The error in  
96 the water balance-based estimates provides a minimum possible error, below which ET  
97 estimation approaches cannot be distinguished due to errors in the underlying reference  
98 data. They found that SFE ET errors are comparable to the error of the catchment water  
99 balances and that SFE outperforms the reanalysis (NARR) and most CMIP6 91 models.

100 However, even this sole gridded implementation of SFE - while promising - is  
101 unable to provide a thorough evaluation of the SFE approach because the comparison  
102 datasets each have their own unquantified uncertainties. Therefore, disagreement  
103 between SFE and CMIP6 cannot be attributed to either dataset because their errors  
104 cannot be distinguished. One solution to this is the statistical evaluation approach of  
105 triple collocation. Using triple collocation and its 7 updated counterpart, extended triple  
106 collocation (McColl et al., 2014), it is possible to compare three datasets with co-located  
107 measurements and estimate two important performance metrics: (1) the variability in the  
108 random error of each dataset and (2) the correlation between the measured value and  
109 the underlying 'true' variable. Both performance metrics can be calculated without  
110 reference to this unknowable 'true' variable, in this case ET, and without assuming the  
111 error of any of the three comparison datasets.

112 Triple collocation - sometimes also referred to as the ‘three-cornered hat’  
113 approach - has been widely used in evaluating datasets where a ‘truth’ or reference  
114 dataset is unavailable, for example in the evaluation of datasets for soil moisture  
115 (Draper et al., 2013; Gruber et al., 2016; Scipal et al., 2008), ocean winds (Caires &  
116 Sterl, 2003), precipitation (Alemohammad et al, 2015, Burnett et al 2020), sensible heat  
117 and carbon fluxes (Alemohammad et al, 2017), ET (Khan et al., 2018), near-surface air  
118 temperature and specific humidity (Sun et al., 2021), and terrestrial water storage  
119 (Ferreira et al., 2016). It can also be used to estimate the coupling of multiple variables,  
120 for example latent heat and soil moisture (Crow et al., 2015). Given three datasets with  
121 observations of the same state variable, each with their own non-correlated random  
122 errors, comparison of the three datasets via triple collocation enables calculation of  
123 each dataset’s random error variance (Stoffelen, 1998).

124 Here, we accomplish two steps in advancing the estimation of ET. First, we  
125 release the first publicly available, gridded dataset of daily SFE ET. We calculate this  
126 dataset at 4 km resolution across the continental United States (CONUS) using  
127 gridMET for 2-m temperature and humidity and net radiation from ERA5-Land. Second,  
128 we compare our gridded estimates of SFE ET to three other remotely sensed ET  
129 estimates: Global Land Evaporation Amsterdam Model Version 4 (GLEAM, Miralles et  
130 al., 2011), FluxCom (Jung et al., 2019), and ERA5-Land (Muñoz-Sabater et al., 2021).  
131 In addition to comparing the spatial pattern and variance of all datasets, we further use  
132 the statistical method of extended triple collocation following McColl et al. (2014) to  
133 calculate the error statistics of each dataset, despite lacking observations of ‘true’ ET  
134 (Gruber et al., 2016; McColl et al., 2014; Stoffelen, 1998).

135

## 136 **2. Methods**

### 137 ***2.1. Calculating ET from atmospheric conditions assuming surface flux*** 138 ***equilibrium***

139 We calculate daily ET after McColl et al. (2019) by assuming that the near-surface  
140 atmosphere is in a state of ‘surface flux equilibrium’ where atmospheric conditions at the  
141 boundary layer reflect the recent fluxes of latent ( $\lambda E$ ) and sensible ( $H$ ) heat on the  
142 Earth’s surface. If this is the case, then increasing ET (i.e. increasing latent heat) will  
143 correspond with diminished sensible heat and result in both atmospheric cooling and  
144 increased humidity. The ratio of sensible and latent heat fluxes - known as the Bowen  
145 ratio ( $B$ ) - can therefore be approximated by temperature and humidity at the boundary  
146 layer, so long as atmospheric conditions reflect the integrated signal of fluxes on the  
147 Earth’s surface.

148 We use 2-m air temperature ( $T_a$ ) and relative humidity ( $q_a$ ) from gridMET  
 149 (Abatzoglou, 2013) to estimate the Bowen ratio, where  $R_v = 461.5$  (J kg<sup>-1</sup> K<sup>-1</sup>) is the  
 150 gas constant for water vapor,  $C_p = 1005$  (J kg<sup>-1</sup> K<sup>-1</sup>) is the specific heat capacity of air  
 151 at constant pressure, and  $\lambda = 2.56 \times 10^6$  (J kg<sup>-1</sup>) is the latent heat of vaporization  
 152 of water (Eq 1).

$$B = \frac{H}{LE} \approx \frac{R_v c_p T_a^2}{\lambda^2 q_a} \quad \text{Eq 1.}$$

153 We choose gridMET because it downscales output from the North American  
 154 Land Data Assimilation System (NLDAS) with PRISM. This incorporation of statistically  
 155 interpolated station data at a fine resolution helps gridMET achieve a high correlation  
 156 with in situ stations, particularly for the variable of temperature, while maintaining a  
 157 relatively fine spatial resolution of 4 km across CONUS (Abatzoglou, 2013). Net  
 158 radiation ( $R_n$ ) allows conversion from the Bowen ratio to ET (Eq 2). We use  $R_n$  from  
 159 ERA5-Land (Muñoz-Sabater et al., 2021) because of its high agreement with in situ  
 160 measurements across CONUS (Yin et al., 2023). However, we note that error in these  
 161 input datasets will propagate to error in the resulting ET estimates.

162 Although the ground heat flux ( $G$ ) can vary from 10% to as much as 50% of  $R_n$   
 163 depending on ground cover (Clothier et al., 1986, Santanello and Friedl, 2003), here we  
 164 assume a constant  $G$  of 10%. Additionally, we do not evaluate SFE ET on any days with  
 165 negative  $R_n$  because doing so would result in a negative ET estimate, which is not  
 166 physical.

$$\lambda ET = (1 + B)^{-1}(R_n - G) \quad \text{Eq. 2}$$

## 167 **2.2 Triple collocation error estimation**

168 Triple collocation assumes a linear error model for each dataset, where the observed  
 169 value for a given dataset ( $x$ ) is assumed to be a linear function of the “true” ET ( $T$ )  
 170 obscured by a constant additive bias ( $\alpha$ ), a constant multiplicative bias ( $\beta$ ) and a  
 171 time-varying additive random error with zero mean ( $\epsilon$ ) (Eq 3). While a linear error model  
 172 likely does not fully capture the error structure of the actual ET dataset errors, it has  
 173 been successfully used to evaluate ET datasets using triple collocation in other regions  
 174 (Kahn et al., 2018, He et al., 2023).

$$x_i = \alpha_i + \beta_i T + \epsilon_i \quad \text{Eq. 3}$$

175 In addition to assuming a linear error model for each dataset, triple collocation  
 176 further assumes that the errors of each dataset are stationary and uncorrelated both  
 177 with each other and with the unknown truth (Gruber et al., 2016; McColl et al., 2014).

178 With these assumptions, the variance of each dataset ( $Q_{11}$ ,  $Q_{22}$ , and  $Q_{33}$ )  
 179 represents the sensitivity of the dataset to variations in the true signal (via the product of  
 180  $\beta_i$  and  $\sigma_T$ ) plus the variance of the random error ( $\sigma_{\epsilon_i}^2$ ) (Eq 4).

$$Q_{ii} = \sigma_i^2 = \beta_i^2 \sigma_T^2 + \sigma_{\epsilon_i}^2 \quad \text{Eq. 4}$$

181 Covariance between pairs of datasets (e.g.  $Q_{12}$ ,  $Q_{13}$ , and  $Q_{23}$ ) likewise provides  
 182 information about each dataset's sensitivity to the true unknown ET via  $\beta_i$  and  $\sigma_T$ . (Eq 5).

$$Q_{ij} = \sigma_{ij}^2 = \beta_i \beta_j \sigma_T^2 \quad \text{Eq. 5}$$

183 The  $\beta_i$  and  $\sigma_T$  terms cancel out for the ratio of each dataset covariance pair,  
 184 resulting in six equations and six unknowns. These can be solved to calculate the  
 185 standard deviation of the random error of each dataset,  $\sigma_\epsilon$  (Eq 6).

$$\sigma_\epsilon = \begin{bmatrix} \sqrt{Q_{11} - \frac{Q_{12}Q_{13}}{Q_{23}}} \\ \sqrt{Q_{22} - \frac{Q_{12}Q_{23}}{Q_{13}}} \\ \sqrt{Q_{33} - \frac{Q_{13}Q_{23}}{Q_{12}}} \end{bmatrix} \quad \text{Eq. 6}$$

186 The absolute values of  $\beta_i$  cannot be separated from the absolute value of  $\sigma_T$ .  
 187 However, many studies assume  $\beta_i = 1$  for one dataset - effectively choosing it as a  
 188 reference dataset which has no multiplicative bias - and calculate  $\beta_i$  for the other two  
 189 datasets *relative* to the actual unknown multiplicative bias of the reference dataset. In  
 190 this study, however, we do not separate  $\beta_i$  and  $\sigma_T$ .

191 Extended triple collocation further allows the calculation of the correlation  
 192 between each dataset and the unknown truth,  $R_T$ , while requiring no additional  
 193 information (McColl et al., 2014); Eq 7).

$$R_T^2 = \begin{bmatrix} \frac{Q_{12}Q_{13}}{Q_{11}Q_{23}} \\ \frac{Q_{12}Q_{23}}{Q_{22}Q_{13}} \\ \frac{Q_{13}Q_{23}}{Q_{33}Q_{12}} \end{bmatrix} \quad \text{Eq. 7}$$

194 Triple collocation requires several assumptions, all of which are likely to be at  
195 least partially violated (e.g., Yilmaz and Crow, 2014). However, these assumptions are  
196 not unique to triple collocation. Gruber et al. (2016) showed that more common  
197 validation strategies implicitly require the same assumptions. For example, if we were to  
198 instead estimate the correlation coefficient and root-mean-squared error (RMSE)  
199 between SFE ET and another reference ET product, we would be implicitly making the  
200 same assumptions.

201

### 202 **2.3. Comparison ET datasets**

203 We compare SFE ET to ET from FluxCom, GLEAM version 4, and ERA5-Land. We  
204 compare all ET datasets over the years 1980 to 2016, which represents the maximum  
205 overlap in temporal coverage between all four datasets. Additionally, we resample each  
206 dataset to match the native resolution of FluxCom at  $0.5^\circ$ . We match the FluxCom  
207 resolution because it is the coarsest. We choose to compare SFE to these particular  
208 three ET datasets not just because they are commonly used, but also to minimize  
209 violation of the triple collocation assumptions, particularly the assumption of  
210 independent errors between datasets. This is commonly achieved by using datasets  
211 that differ in their input data sources and modeling frameworks (Gruber et al., 2016;  
212 McColl et al., 2014). We also remove the seasonal cycle from each dataset by  
213 subtracting the 30-day rolling average from each day (Chen et al., 2018; Draper et al.,  
214 2013; Miralles et al., 2010). This ensures that differences in the seasonality and timing  
215 of ET do not impact the triple collocation analysis and has been shown to improve error  
216 estimation with triple collocation for ET datasets specifically (He et al., 2023).  
217 Performing triple collocation on the anomaly should also reduce violation of the  
218 assumption that the ET error structure is linear. This is because the low-frequency (e.g.  
219 seasonal) ET signals which are removed are expected to have a different non-linearity  
220 than the high-frequency signals isolated by the anomaly (Miralles et al., 2010, Su et al.,  
221 2014).

222 After removing the seasonal cycle, we choose only the months of March through  
223 October for the triple collocation analysis. This is because negative daily net radiation  
224 occurs for some pixels during the winter months, prohibiting the calculation for SFE.  
225 Because the number of days with negative net radiation varies for each pixel, we  
226 eliminate all winter months for all datasets to ensure a consistent number of data for  
227 each dataset and pixel.

228 Finally, we use extended triple collocation to calculate the standard deviation of  
229 the random error and the correlation coefficient of each dataset (see Sec 2.2 above).  
230 Because we have four comparison datasets and triple collocation requires just three, we  
231 are able to repeat our estimates of each dataset's error statistics once for each possible

232 'triplet' (i.e. combination) of three datasets. Convergence of the error estimates  
233 regardless of the triplet chosen increases our confidence in the robustness of the triple  
234 collocation assumptions and therefore in our calculated values (Draper et al., 2013; He  
235 et al., 2023). In addition to performing triple collocation, we also compare the four  
236 datasets via a general analysis of the variance and spatial patterns of ET.

237         The FluxCom dataset we choose for our triple collocation analysis uses machine  
238 learning to upscale eddy covariance measurements from flux towers based on satellite  
239 and meteorological inputs. FluxCom provides an ensemble of latent heat estimates  
240 trained using different meteorological datasets. In order to have the longest data record  
241 with daily resolution, here we use the single FluxCom ensemble member trained with  
242 the CRUNCEPv6 reanalysis product (Wei et al., 2014), as opposed to the mean of all  
243 possible FluxCom ensemble members. However, the different model setups (each with  
244 a different weather model) were previously found to have similar performance (Jung et  
245 al., 2019). In addition to the climate data from CRUNCEP, FluxCom uses radiation data  
246 from CERES (Doelling et al., 2013), precipitation from the Global Precipitation  
247 Climatology Project (GPCP, Huffman et al., 2001), and temperature, land cover, and  
248 other reflectance indicators from MODIS. The FluxCom model is run per plant functional  
249 type and then combined into a single estimate by weighting each plant functional type's  
250 fractional areal coverage of the pixel (Jung et al., 2019).

251         GLEAM estimates ET by using remote sensing and reanalysis data to force a  
252 hybrid model which includes modules for canopy interception, potential  
253 evapotranspiration, soil water content, and vegetation response to evaporative stress.  
254 Although FluxCom and GLEAM have some remote sensing inputs in common, for  
255 example radiation from CERES and vegetation information from MODIS, GLEAM Version  
256 4 takes a hybrid modelling approach and does not rely fully on machine learning like  
257 FluxCom. Specifically, GLEAM version 4 primarily uses physical modelling modules with  
258 only a single module – for evaporative stress – using a deep neural network trained  
259 using in situ data from eddy covariance towers and sap flow measurements (Koppa et  
260 al., 2022; Martens et al., 2017; Miralles et al., 2025). This is in contrast to GLEAM  
261 version 3, which estimates evaporative stress empirically as a function of soil moisture  
262 and vegetation optical depth - both from microwave remote sensing inputs. Additionally,  
263 GLEAM Version 4 calculates ET using Penman's equation (as opposed to  
264 Priestley-Taylor, used in Version 3) and also updates the multi-layer water balance  
265 model so that vegetation access to groundwater can be represented. However, in  
266 GLEAM Version 4, plant rooting depths are static for each land cover within the  
267 groundwater scheme and there is still a prescribed multiplicative stress function to  
268 determine how vegetation responds to soil moisture stress. GLEAM is the only dataset  
269 in our comparison set which partitions ET between evaporation, transpiration, and

270 interception. We use the variable referring to the total evaporation (E) to best match the  
271 other ET estimates.

272 Finally, ERA5-Land uses the near-surface atmospheric reanalysis from ERA5,  
273 which assimilates observations from a range of satellites and in situ observation  
274 networks for many variables including land surface temperature, precipitation, wind  
275 speed, and soil moisture (Hersbach et al., 2020). ERA5-Land then takes the  
276 atmospheric states from ERA5 and re-runs the land surface model component at a finer  
277 resolution (9 km) offline (Muñoz-Sabater et al., 2021). This allows for additional and  
278 refined land surface parameterizations and corrections. Unlike FluxCom and GLEAM,  
279 ERA5-Land has no machine learning components. For our analysis, we sum the hourly  
280 latent heat flux output of ERA5-Land to daily totals and then resample bilinearly to  
281 match the coarser 0.5° FluxCom grid. Finally, both ERA5-Land and FluxCom report  
282 latent heat flux in units of energy per unit area, which we convert to ET (mm/day) by  
283 dividing by the latent heat of vaporization ( $\lambda = 2.56 \times 10^6 \text{ J kg}^{-1}$ ).

284

#### 285 **2.4. Comparing performance across biogeographical factors**

286 We compare the resulting  $\sigma_\epsilon$  and  $R_T$  estimates from triple collocation across a variety of  
287 biogeographical factors - specifically climate, elevation, land cover type, and the  
288 distance to the coast - to better understand under what conditions SFE ET performs  
289 well and how its performance across biogeography compares to that of the other ET  
290 estimates.

291 We calculate the mean annual precipitation at each pixel using monthly  
292 precipitation (P) from 1991 to 2020 from TerraClimate (Abatzoglou, 2013). We use  
293 elevation from MERIT Hydro (Version 1.0.1., (Yamazaki et al., 2019). For land cover, we  
294 use the National Land Cover Database (NLCD) land cover map from 2021 (Dewitz,  
295 2024). We consider the land cover types of forest (combining deciduous, evergreen,  
296 and mixed forests), shrub, grassland, wetland (combining woody and herbaceous  
297 wetlands), and agricultural (cultivated crops).

298 We further analyze the performance of each dataset by each pixel's distance  
299 from the coast because the assumptions of SFE are likely to be violated near the ocean  
300 (McColl et al., 2019). This is because in coastal regions, ocean moisture and  
301 temperature are expected to be a strong control on land surface fluxes. We calculate  
302 the distance of each pixel centroid from the nearest coast using the TIGER/Line  
303 Coastline National Shapefile (United States Census Bureau, 2019). We also exclude  
304 pixels from all analyses if their centroid overlaps with the ten largest water bodies in  
305 CONUS (ArcGIS Data and Maps, 2023).

306

### 307 **3. Results**

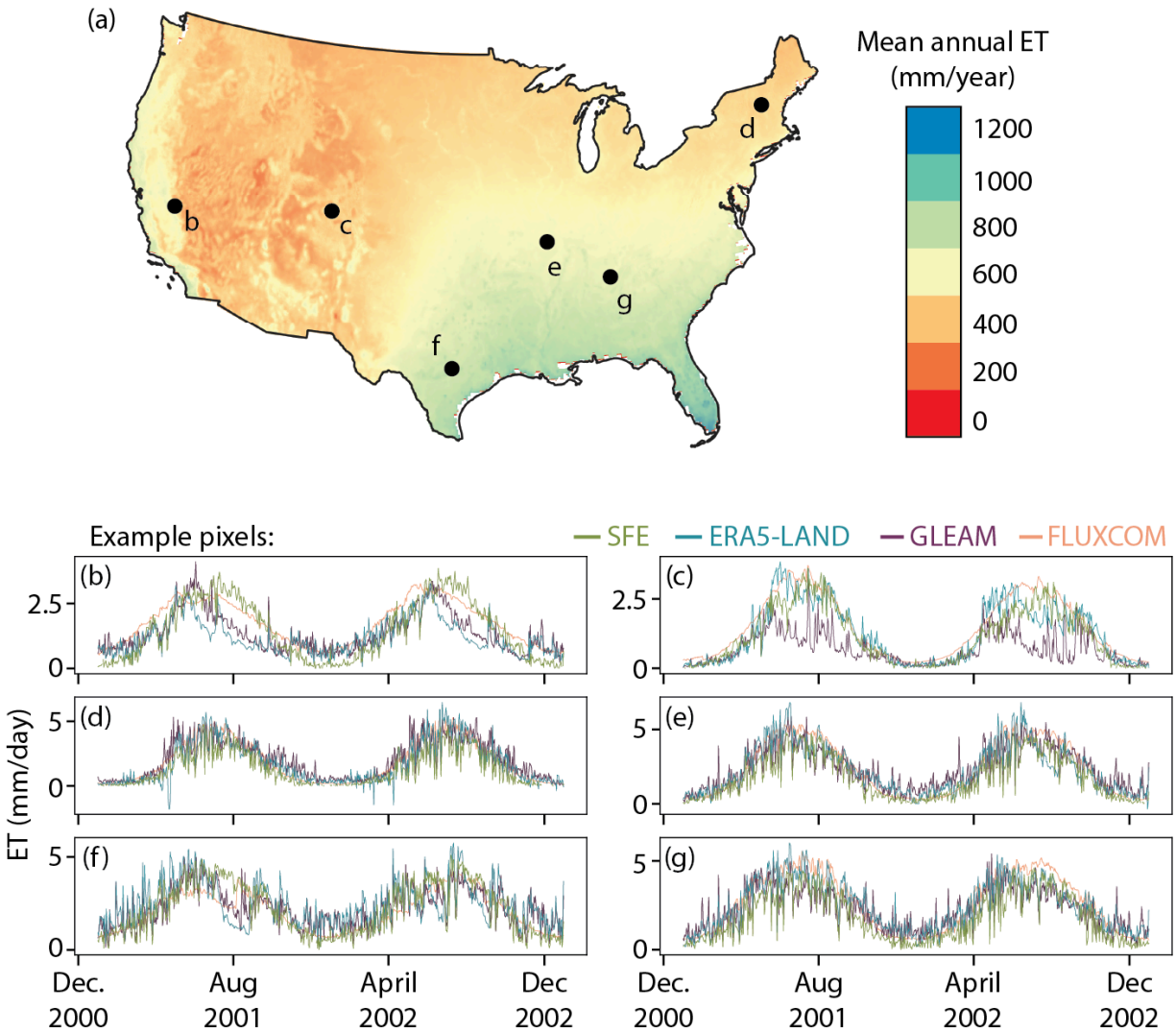
#### 308 **3.1. Surface flux equilibrium ET across CONUS from 1979 to 2025**

309 Here, we publicly release a dataset of daily SFE ET from 1979 to 2025 at 4 km  
310 resolution across CONUS (see Data Availability section). The spatial mean (shown in  
311 Figure 1a) follows expected patterns across CONUS - with an aridity driven gradient  
312 from West to East and a radiation driven gradient from North to South in the Eastern  
313 US. This spatial pattern exists regardless of the choice of parameter for the ground heat  
314 flux ( $G$ ), although the magnitude of mean annual ET is altered (Figure S1). The temporal  
315 variability in daily ET calculated using the SFE approach is consistent with the  
316 comparison datasets (Figure S2). However, SFE has a larger standard deviation across  
317 much of CONUS - particularly the Western US - than FluxCom and GLEAM. Across  
318 several sample pixels, chosen as heavily vegetated examples spanning multiple  
319 regions, the seasonal cycle of mean annual ET is likewise comparable across all four  
320 ET estimates, although the timing of maximum summer ET each year varies between  
321 datasets (Figure 1b-g).

322 The magnitude of mean annual continental SFE ET (Figure 2) and the pattern of  
323 interannual variability which matches SFE the best is that of GLEAM ( $\rho = 0.55$ ). The two  
324 datasets with the overall closest match in ET interannual variability, however, are  
325 FluxCom and ERA5-Land ( $\rho = 0.71$ ). All correlation coefficients are shown in Table S1.  
326 Although SFE and FluxCom each have intermediate magnitudes of mean continental  
327 ET relative to GLEAM and ERA5, both datasets - and FluxCom in particular - also have  
328 the lowest interannual variability magnitude (8 mm/year standard deviation for FluxCom  
329 and 10.5 mm/year for SFE, compared to 22 and 28 mm/year for ERA5-Land and  
330 GLEAM, respectively). Across the entire average record, the mean annual ET from SFE  
331 (538 mm/yr) is just below GLEAM (552 mm/yr), with ERA5-Land having the highest  
332 mean annual ET (645 mm/yr). The mean annual ET across CONUS is shown in Table  
333 S2.

334

335

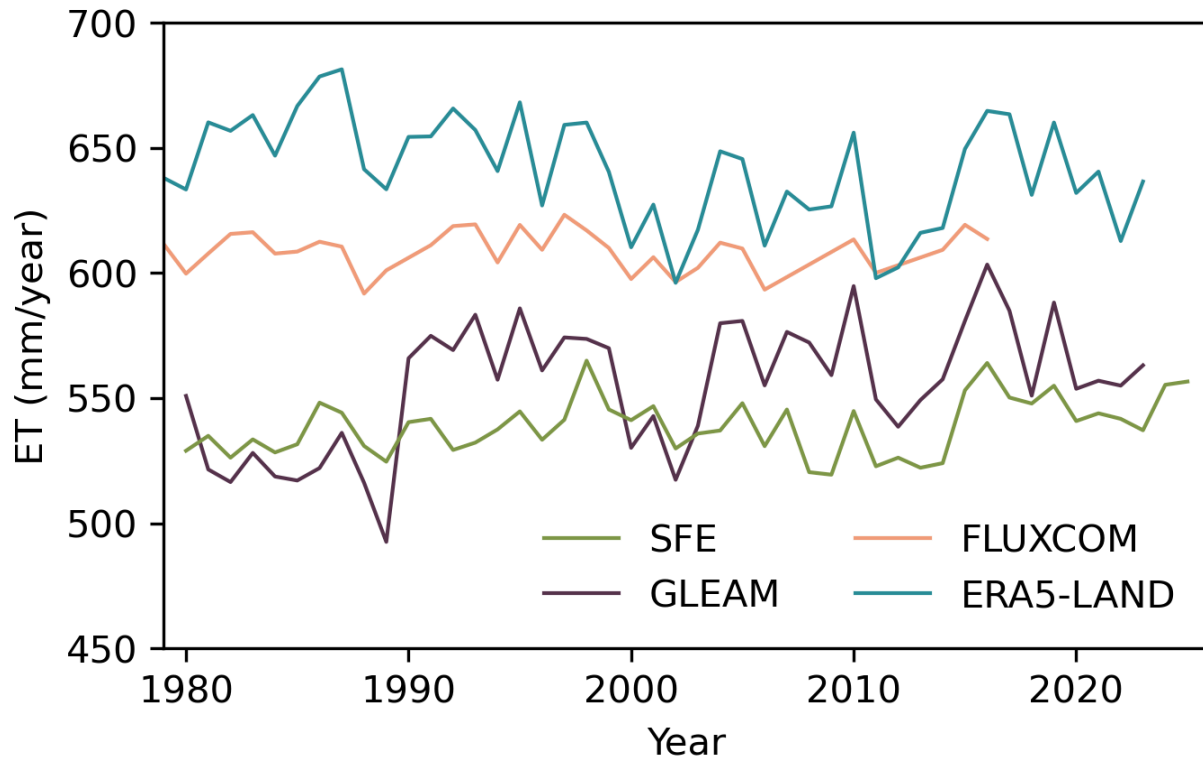


336

337 Figure 1. Mean annual SFE ET across CONUS from 1979 to 2025. Points show  
 338 timeseries for example pixels for SFE (green), ERA5-Land (blue), GLEAM (purple) and  
 339 FluxCom (pink).

340

341



342

343 *Figure 2. Interannual variability in mean annual ET across CONUS from 1979 through*  
 344 *the record length of each dataset.*

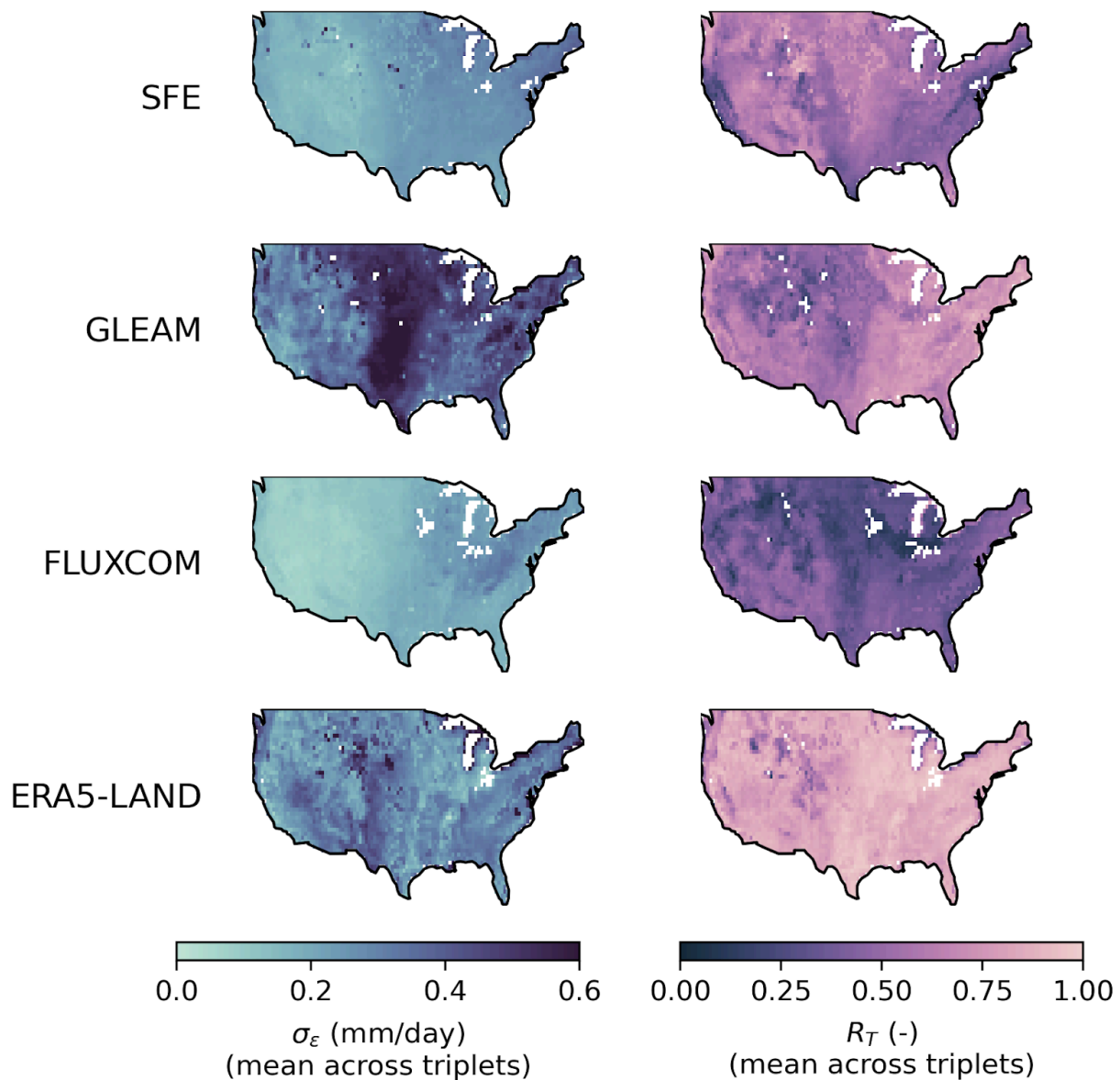
345

346 **3.2. SFE is the only dataset that performs well in terms of both the standard**  
 347 **deviation of the random error and the correlation coefficient**

348 SFE performance during non-winter months as estimated by triple collocation is  
 349 comparable - and even exceeds - the performance of the comparison datasets across  
 350 much of CONUS, despite its extreme simplicity, lack of tunable parameters, and  
 351 relatively small number of assumptions (Figure 3). SFE, FluxCom, and GLEAM show a  
 352 strong divide in performance between the Western and Eastern US. SFE and FluxCom  
 353 both have the lowest  $\sigma_\epsilon$  and highest  $R_7$  in the Western US compared to the Eastern US.  
 354 In contrast, GLEAM has lower  $\sigma_\epsilon$  in the Western US, but higher  $R_7$  in the Eastern US.  
 355 ERA5-Land shows more heterogeneity in performance across space - especially  
 356 compared to SFE and FluxCom - and has no clear performance gradient between the  
 357 Western and Eastern US.

358

359



360

361 *Figure 3. The standard deviation of the random error,  $\sigma_\epsilon$  (left) and correlation coefficient*  
 362 *to the truth,  $R_T$  (right) for each dataset averaged across all triplet combinations.*

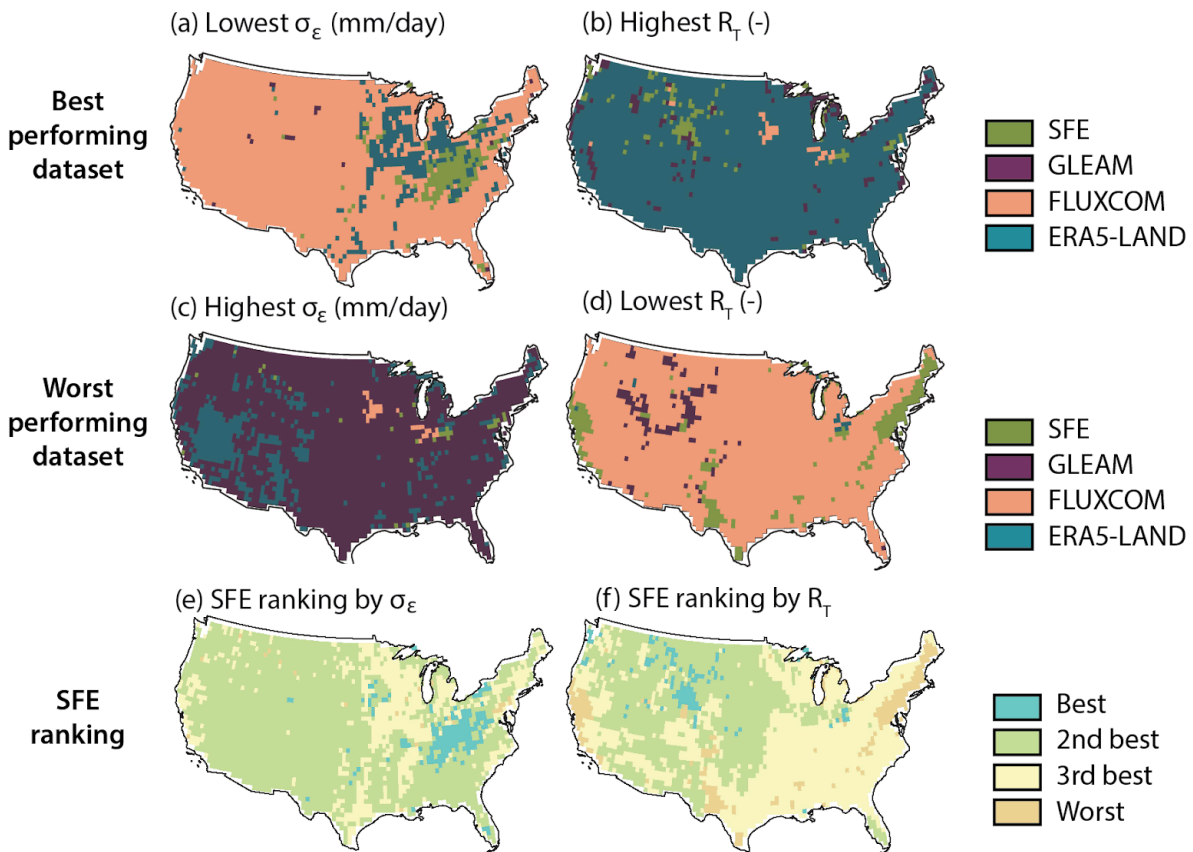
363 *Increasingly light colors are better performance. White pixels have no valid data for any*  
 364 *triplet.*

365

366 Despite its simplicity, SFE is the best or second-best dataset according to both  $\sigma_\epsilon$   
 367 and  $R_T$  across more than half of CONUS (Figure 4). SFE has the lowest or second  
 368 lowest  $\sigma_\epsilon$  and highest or second highest  $R_T$  across 46.1% and 77.9% of pixels across  
 369 CONUS, respectively (Figure 4, Table 1), mostly in the Western US.

370 SFE's high performance with regards to both  $\sigma_\varepsilon$  and  $R_T$  is unique among the  
 371 comparison datasets. Other than SFE, the datasets with the best  $\sigma_\varepsilon$  and  $R_T$ ,  
 372 respectively, have the lowest performance for the complementary metric. For example,  
 373 FluxCom has the lowest  $\sigma_\varepsilon$  across the majority of CONUS, but it also has the lowest  $R_T$   
 374 (Figure 4). The opposite is true for ERA5, which is the highest performing dataset  
 375 according to  $R_T$  across much of CONUS but frequently has the worst performance  
 376 according to  $\sigma_\varepsilon$ , particularly in the US Southwest. SFE is the only dataset which  
 377 consistently has high performance according to both metrics.

378



379

380 *Figure 4. Summary of relative performance of all four datasets. The dataset with highest*  
 381 *performance for the standard deviation of the random error,  $\sigma_\varepsilon$  (a) and the correlation*  
 382 *coefficient with 'true' ET,  $R_T$  (b) for each pixel. The worst performing datasets for  $\sigma_\varepsilon$  (c)*  
 383 *and  $R_T$  (d). The relative ranking of SFE for  $\sigma_\varepsilon$  (e) and  $R_T$  (f). The total number of pixels*  
 384 *(and relative percent of pixels) of each color are shown in Table S1. Pixels with*  
 385 *centroids within 4 km of the border have been removed.*

386

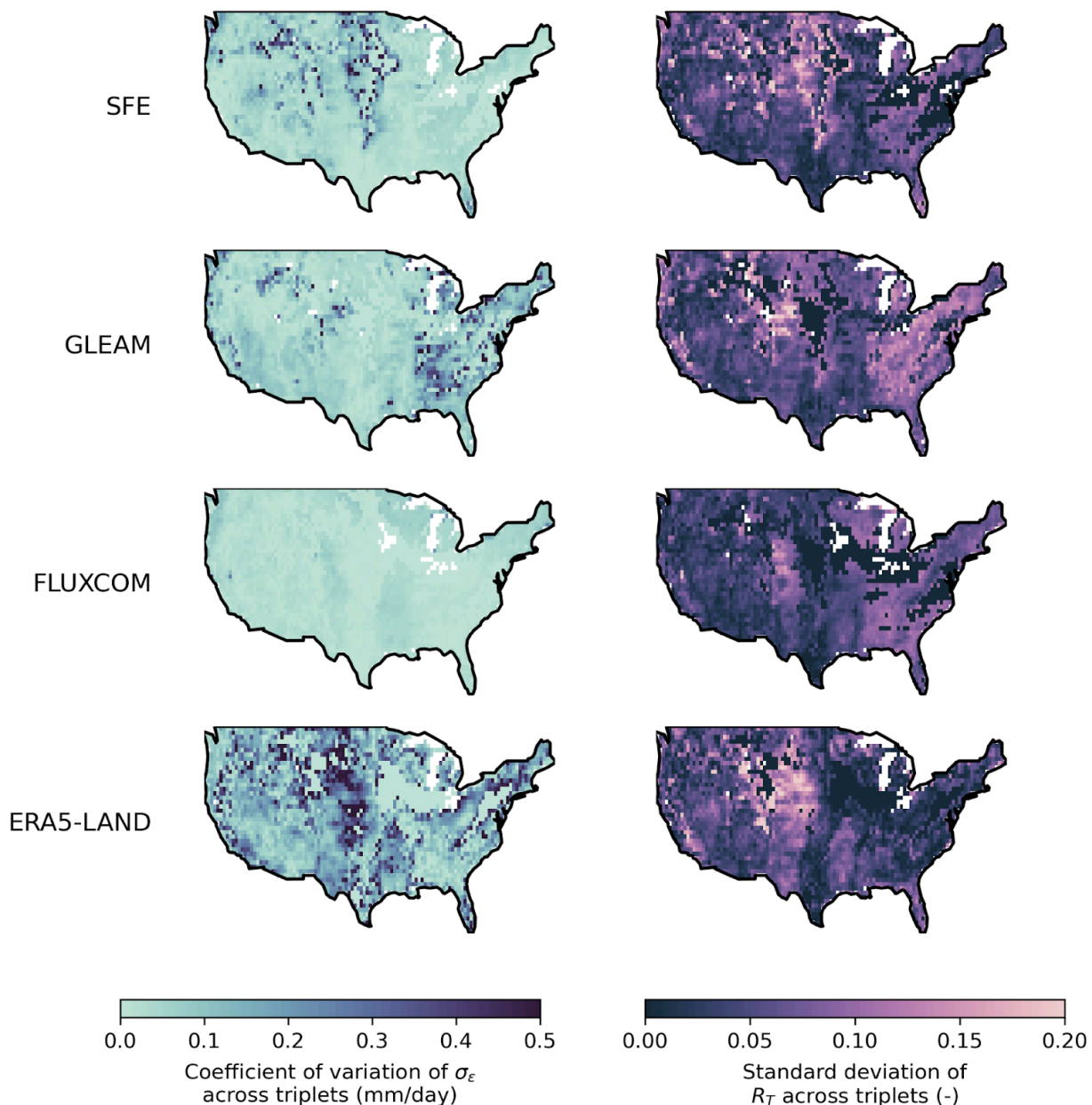
387

388 Table 1. (Top) The number of pixels where each dataset has the best performance  
 389 according to the standard deviation of the random error,  $\sigma_\varepsilon$ , and the correlation  
 390 coefficient to the truth,  $R_T$ . (Bottom) The number of pixels by SFE ET ranking.

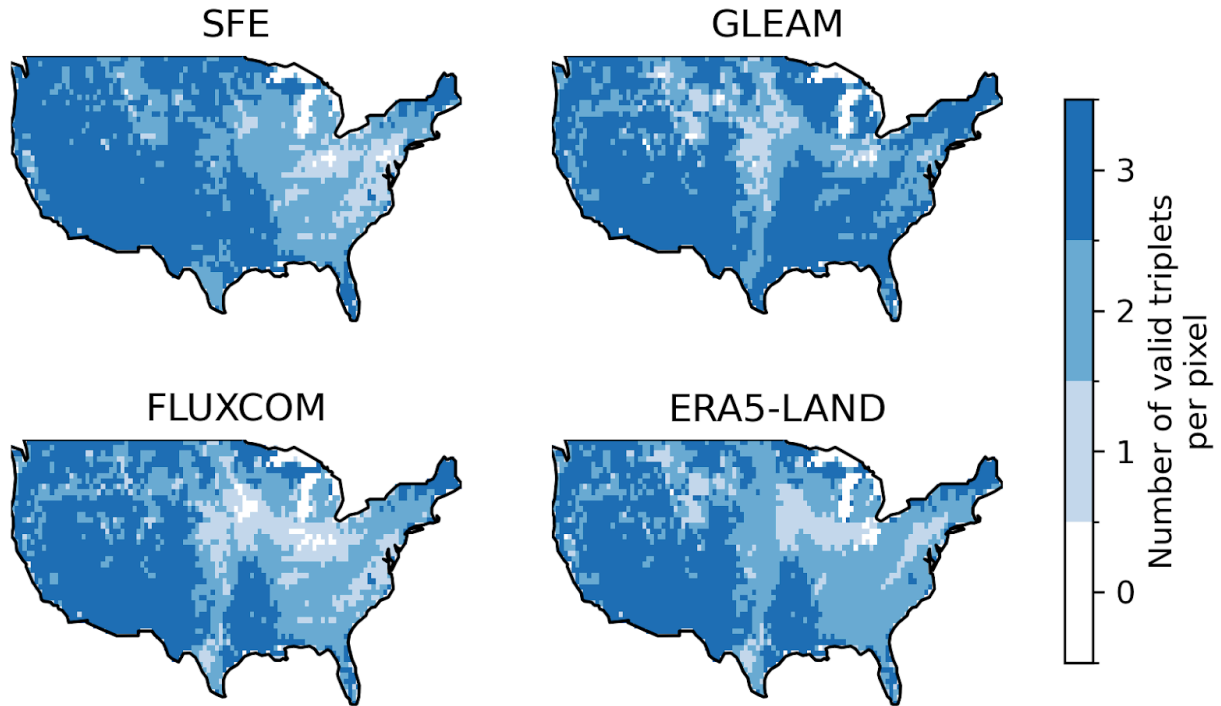
Best dataset				
	By $\sigma_\varepsilon$		By $R_T$	
	Pixels	Percent	Pixels	Percent
SFE	164	(5.4%)	115	(3.8%)
GLEAM	17	(0.6%)	159	(5.2%)
FLUXCOM	2537	(83.7%)	33	(1.1%)
ERA5-Land	314	(10.4%)	2725	(89.9%)
Ranking of SFE				
	By $\sigma_\varepsilon$		By $R_T$	
	Pixels	Percent	Pixels	Percent
1st	111	(3.7%)	156	(5.1%)
2nd	1286	(42.4%)	2206	(72.8%)
3rd	1397	(46.1%)	646	(21.3%)
4th	238	(7.8%)	24	(0.8%)

409 We note that the estimates of  $\sigma_\varepsilon$  and  $R_T$  are consistent between triplets,  
 410 indicating  $\sigma_\varepsilon$  and  $R_T$  estimates are robust to the choice of comparison datasets (Figure  
 411 5). Individual  $\sigma_\varepsilon$  and  $R_T$  maps for each dataset and triplet combination are shown in  
 412 Figures S3 and S4 and differences between each triplet combination are shown in  
 413 Figures S5 and S6. However, not all pixels have valid results for each triplet  
 414 combination, which occurs when either  $\sigma_\varepsilon$  is negative for one or more of the datasets or  
 415 if any  $R_T$  are greater than one. Figure 6 shows the total number of triplets which are  
 416 valid for each pixel. The triplets with the most invalid pixels are those where FluxCom  
 417 and ERA5-Land are both included. Invalid pixels are also more common in the Eastern  
 418 US rather than the Western US. Even in the East, however, SFE - our main estimate of  
 419 interest - still has at least one valid triplet in 96% of pixels and at least two valid triplets  
 420 in 88% of pixels. SFE has three valid triplets - the maximum possible number for our  
 421 four dataset analysis - in 56% of pixels. The triple collocation results are also relatively  
 422

423 insensitive to the choice of the ground heat flux ( $G$ ) parameter used in the calculation of  
 424 SFE, although increases in  $G$  necessarily reduce ET estimates, and therefore also  
 425 reduce  $\sigma_\epsilon$  (Figure S7). To the extent that uncertainty in  $G$  causes errors in the SFE ET  
 426 estimate, it will also cause errors in estimates from other ET products, which must make  
 427 similar assumptions or approximations for  $G$ .



428  
 429 *Figure 5. (left) The coefficient of variation of  $\sigma_\epsilon$  for each dataset across all possible*  
 430 *triplet combinations with valid data. White pixels have no valid data for any triplet. (right)*  
 431 *The standard deviation of  $R_T$  for each dataset across all possible triplet combinations*  
 432 *with valid data. White pixels have no valid data for any triplet and black pixels have only*  
 433 *one triplet combination with valid data.*



434

435 *Figure 6. The total number of triple collocation estimates - one from each possible*  
 436 *combination of datasets - that are averaged for each pixel and dataset combination.*  
 437 *Pixels with no valid triple collocation results for any triplet are shown in white. The*  
 438 *maximum number of valid triplets is three.*

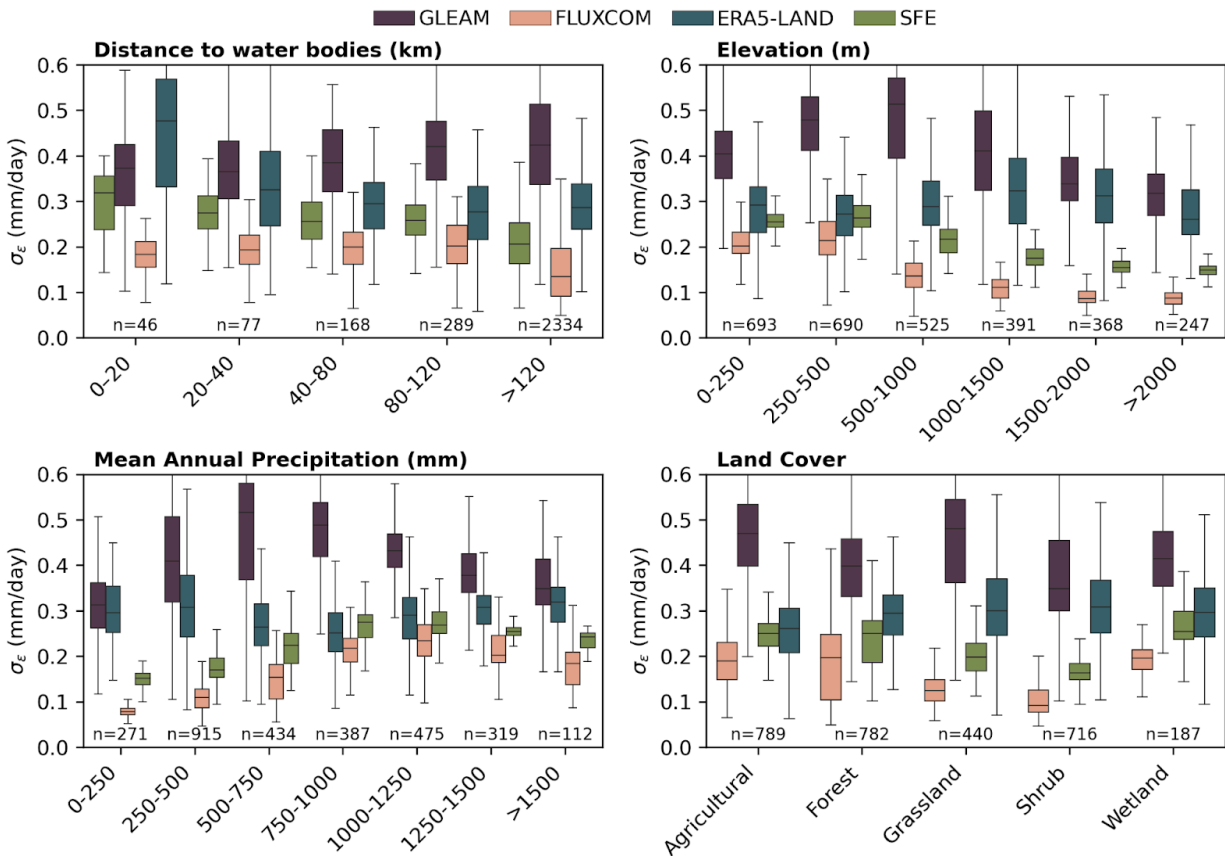
439

### 440 **3.3. Performance across biogeographical factors**

441 Comparing the trends of  $\sigma_\epsilon$  (Figure 7) and  $R_T$  (Figure 8) across mean annual  
 442 precipitation, elevation, landcover, and the distance to large water bodies shows that  
 443 SFE performance is not more sensitive to any of these biogeographical factors than the  
 444 comparison datasets. Even when comparing SFE performance with coastal proximity -  
 445 a factor where we expect to see performance degradation due to the violation of SFE  
 446 assumptions (McColl and Rigden, 2020) - the coastal proximity penalty of SFE is  
 447 comparable to that of ERA5-Land. Indeed, ERA5-Land shows the sharpest decrease in  
 448 performance within 20 km of the coast out of any of the datasets, however both SFE  
 449 and ERA5-Land continue to show improved performance even up to 120 km inland.  
 450 Neither GLEAM nor FluxCom have a strong relationship between coastal proximity and  
 451 performance.

452 Likely due to its correlation with coastal proximity, SFE also has decreased  
 453 performance at lower elevations with respect to both evaluation metrics. FluxCom and  
 454 GLEAM likewise show their highest  $\sigma_\epsilon$  at low elevations relative to higher elevations,  
 455 with FluxCom  $\sigma_\epsilon$  peaking around 500 m a.s.l. and GLEAM  $\sigma_\epsilon$  around 1000 m. a.s.l. All

456 three datasets continue to have decreased  $\sigma_\varepsilon$  as elevation increases. The relationship  
 457 between elevation and  $R_T$  is relatively flat for SFE and FluxCom in the intermediate  
 458 elevations, with the lowest  $R_T$  at the extreme low and high elevations. GLEAM and  
 459 ERA5, however, have continuously decreasing  $R_T$  with increasing elevation, and the  
 460 lowest  $R_T$  at elevations exceeding 2000 m a.s.l.



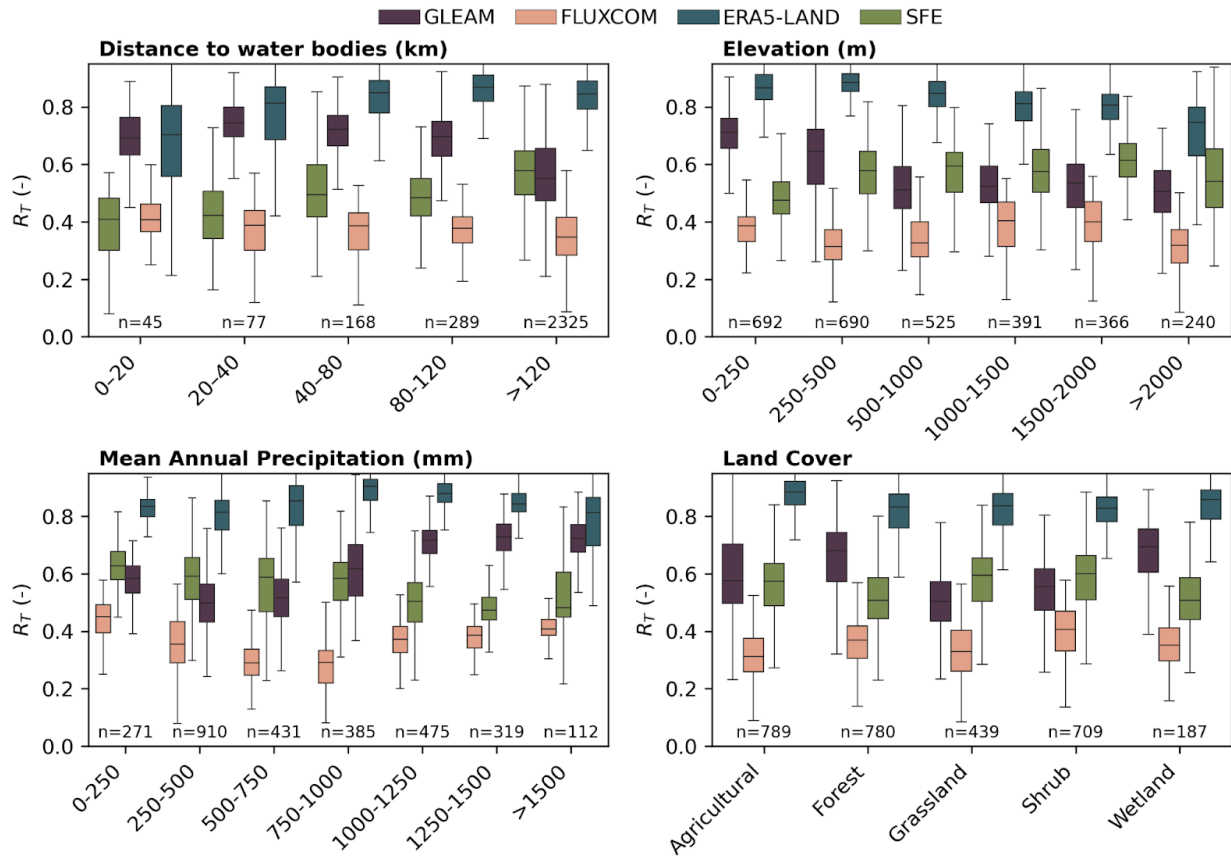
461

462 *Figure 7. The standard deviation of the random error,  $\sigma_\varepsilon$ , for each ET dataset across*  
 463 *mean annual precipitation, the distance to large water bodies, elevation, and land cover.*  
 464 *The number of pixels in each category per ET dataset is shown below boxes.*

465

466 The  $\sigma_\varepsilon$  for SFE, GLEAM, and FluxCom is lowest at the driest and wettest pixels  
 467 and highest at pixels with intermediate precipitation. However, the  $\sigma_\varepsilon$  for GLEAM peaks  
 468 at the 500- 750 mm/year bin whereas FluxCom and SFE have the highest  $\sigma_\varepsilon$  at slightly  
 469 wetter locations, receiving between 1000-1250 mm/year. ERA5-Land, on the other  
 470 hand, has a weaker relationship between mean annual precipitation and  $\sigma_\varepsilon$ . ERA5-Land  
 471 has the opposite pattern than the other datasets and shows the highest  $\sigma_\varepsilon$  at the driest  
 472 and wettest pixels with lower  $\sigma_\varepsilon$  at intermediate aridity. The relationship between mean  
 473 annual precipitation and  $R_T$  follows that of mean annual precipitation and  $\sigma_\varepsilon$  in general,

474 however  $R_T$  does not increase at the wettest pixels to the same degree as for the  $\sigma_\varepsilon$ . For  
 475 example, SFE has continually decreasing  $R_T$  as mean annual precipitation increases  
 476 with only a minimal increase in performance at the pixels with >1500 mm/year of  
 477 precipitation.



478  
 479 *Figure 8. The correlation coefficient,  $R_T$ , for each ET dataset across mean annual*  
 480 *precipitation, the distance to large water bodies, elevation, and land cover. The number*  
 481 *of pixels in each category per ET dataset is shown below boxes.*

482

483 The performance variability across land cover is not consistent between any of  
 484 the datasets. ERA5-Land has the lowest  $\sigma_\varepsilon$  and highest  $R_T$  in agricultural pixels,  
 485 GLEAM in forest pixels, and FluxCom in shrubland pixels. The SFE  $R_T$  is similar across  
 486 all land cover types but SFE  $\sigma_\varepsilon$  is highest in wetlands, followed by forest and agricultural  
 487 pixels. Forested pixels also have a greater spread in  $\sigma_\varepsilon$  for FluxCom and SFE compared  
 488 to the other land cover types. SFE  $\sigma_\varepsilon$  is lowest in shrublands, followed by grasslands.  
 489 FluxCom  $\sigma_\varepsilon$  is likewise lowest for grassland and shrublands, which is the opposite of  
 490 ERA5-Land, with the highest  $\sigma_\varepsilon$  in grasslands and shrublands.

491

## 492 **4. Discussion**

### 493 **4.1. Which ET estimate is most accurate?**

494 While triple collocation reveals that SFE is rarely the highest performing dataset for the  
495 non-winter months evaluated here, it is the second-best performing dataset across  
496 much of CONUS for both  $\sigma_\epsilon$  and  $R_T$  (Figure 4e,f). In addition, we find that datasets  
497 which outperform SFE only exhibit better performance for one - not both - of either  $\sigma_\epsilon$   
498 and  $R_T$ . That SFE performs well - although not the best - for both metrics suggests its  
499 usefulness for a variety of applications, particularly those where it is not clear a priori  
500 whether having high  $R_T$  or low  $\sigma_\epsilon$  is most useful. Furthermore, SFE may be a particularly  
501 good choice for studies interested in the response of ET to water limitations. Unlike the  
502 explicitly assumed dependence of ET on hydrologic conditions in ERA5-Land or the  
503 implicitly assumed dependence of GLEAM and FluxCom (which is limited by the  
504 constraints of the machine learning structure and input data), SFE contains no a priori  
505 assumptions about the effect of water stress on ET, aside from any impact of these  
506 assumptions embedded in the interpolated temperature or humidity data used as an  
507 input to SFE calculation (such as for the gridMET data used here). Our release,  
508 alongside this manuscript, of a daily, 4km resolution CONUS-wide dataset of  
509 SFE-based ET spanning 1979 to 2025 should facilitate future applications of SFE for  
510 scientific analyses. Additionally, there is no reason to believe that SFE should not  
511 perform similarly at the global scale, particularly outside of regions with substantial  
512 influence from ocean dynamics.

513 SFE is generally the second-best dataset regardless of metric, while alternative  
514 datasets with low random noise also have low correlation with the truth and vice versa.  
515 For example, across the four datasets tested, FluxCom has the lowest (most desirable)  
516  $\sigma_\epsilon$  across the majority of CONUS pixels (Figure 4a). However, it also has the lowest  
517 (least desirable)  $R_T$  more often than any other datasets (Figure 4d). ERA5-Land shows  
518 the converse relationship, with the highest (most desirable)  $R_T$  in almost all pixels  
519 compared to all other datasets, but poorer relative performance with regard to  $\sigma_\epsilon$   
520 (Figure 4b,c). How is this possible? To understand why, note that the triple collocation  
521 error model implies that,

$$R_{T,i}^2 = \frac{\beta_i^2 \sigma_T^2}{\beta_i^2 \sigma_T^2 + \sigma_{\epsilon,i}^2} \quad \text{Eq. 8}$$

522 as shown in McColl et al. (2014). For a dataset to exhibit both the lowest  $R_T$  and lowest  
523  $\sigma_\epsilon$  requires that  $\beta$  is also sufficiently small ( $\sigma_T$  is the same for each dataset and does not  
524 impact the ranking). An extreme example would be a dataset that simply set ET to a  
525 fixed climatological value and exhibited no temporal variability, for which  $\beta = 0$  and  $R_T =$   
526 0, even when  $\sigma_\epsilon$  is small. At the other extreme, for a dataset to exhibit both highest  $R_T$

527 and highest  $\sigma_\varepsilon$  requires  $\beta$  to be sufficiently large. In the limit of  $\beta \rightarrow \infty$ ,  $R_T = 1$ , even  
528 when  $\sigma_\varepsilon$  is large. The relative importance of choosing a dataset with a low  $\sigma_\varepsilon$ , a high  $R_T$ ,  
529 or a low bias (which is not assessed here), depends on the application for which the ET  
530 dataset will be used (Entekhabi et al., 2010).

531 Beyond choosing a single dataset for a particular application, it is also possible to  
532 average multiple ET estimates into a single dataset weighted by each dataset's  
533 performance. While not often practical for large-scale use, He et al., (2023) used triple  
534 collocation to estimate an 'optimal' ET product over China by weighting each dataset by  
535 the performance of the triple collocation results in order to minimize  $\sigma_\varepsilon$ . Burnett et al  
536 (2020) also used this approach to generate a new rainfall product for the Congo River  
537 Basin. Such an approach was also proposed as a possible way forward by the WAter  
538 Cycle Multi- mission Observation Strategy (WACMOS) project, with the specific  
539 suggestion that ET datasets could be combined on a per-biome scale, if some datasets  
540 are known to perform better or worse under specific conditions (Miralles et al., 2016).  
541 However, this approach has the disadvantage of obscuring the individual problems with  
542 each dataset, especially if the datasets have different systematic errors or biases which  
543 are not accounted for by the random error variance and correlation coefficient metrics  
544 available through triple collocation analysis.. It may also perturb the larger-scale spatial  
545 patterns of ET. Given that the validity of the assumptions behind triple collocation are  
546 not fully known, any such effort would benefit from additional corroboration of the  
547 estimated uncertainties.

548

#### 549 **4.2. Do spatial patterns in SFE performance match our expectation?**

550 We find that the performance of SFE is not more sensitive to biogeographical gradients  
551 than that of other datasets, suggesting that the simplicity of SFE does not exacerbate  
552 performance issues for specific climate, vegetation, or topographical environments. This  
553 is particularly surprising given the previously hypothesized limitation of SFE in coastal  
554 regions, where atmospheric conditions strongly depend on the influence of the ocean as  
555 well as on recent land fluxes (McColl and Rigden, 2020). However, the SFE method has  
556 not previously been applied within 250 km of the coast, let alone had its errors  
557 characterized in these regions. Therefore, the actual performance of SFE in coastal  
558 regions has previously remained unknown.

559 While our statistical analysis (Figure 7, Figure 8) shows the expected increase in  
560 SFE  $\sigma_\varepsilon$  and reduction in  $R_T$  near the coast, particularly within the first four pixels (~20  
561 km), this behavior is also true for ERA5-Land, which has even more severe  
562 performance decreases near the coast than SFE. This is despite the improved  
563 simulation of land surface temperature and surface energy fluxes in ERA5-Land  
564 compared ERA5 for coastal regions, which has been mainly attributed to ERA5-Land's

565 finer spatial resolution (Martens et al., 2020; Muñoz-Sabater et al., 2021). However,  
566 ERA5-Land performance is not uniformly degraded for all coastal areas (Figure 3).  
567 Instead, coastal areas in the North show higher  $\sigma_\varepsilon$  and  $R_T$  compared to coastal areas in  
568 the Southwest and Southeast. This might suggest that the statistically lower  
569 performance of ERA5 Land with coastal proximity in general is due to cross correlation  
570 with other climatic factors. Despite the decreased performance of SFE and ERA5-Land  
571 near the coast, however, the absolute magnitude of  $\sigma_\varepsilon$  and  $R_T$  for both datasets is still  
572 comparable to those of the other datasets throughout the range of coastal proximities,  
573 particularly for  $\sigma_\varepsilon$ . Therefore, coastal proximity may not necessarily limit the usefulness  
574 of SFE near coasts. Future SFE implementation and evaluation studies should further  
575 investigate these limitations and not exclude areas within 250 km of the coast a priori.

576 SFE has the highest  $\sigma_\varepsilon$  at low elevations, as does GLEAM and FluxCom.  
577 Spatially, however, topographical gradients (such as around the Rocky Mountains) are  
578 not apparent on maps of  $\sigma_\varepsilon$  for any of the datasets (Figure 3), although several smaller  
579 mountain ranges (e.g. the Sierra Nevada in California and the upper Appalachian  
580 Mountains) do show lower performance for the  $R_T$  of SFE and FluxCom. This lack of  
581 coherence between the elevation trends and spatial patterns could indicate cross  
582 correlation between elevation and other factors impacting performance, which require  
583 further investigation.

584 The most obvious spatial trend in dataset performance is the gradient of  
585 performance between the Eastern and Western US. SFE and FluxCom have lower  $\sigma_\varepsilon$  in  
586 the Western US than in the East, despite the Western US being well-known as a region  
587 where ET estimation is difficult. One possible explanation for our results is that ET  
588 amounts are lower in the West, where vegetation cover is in general lower and aridity  
589 higher, such that the overall magnitudes of  $\sigma_\varepsilon$  are also lower. This would also explain the  
590 lack of systematic difference in FluxCom and SFE  $R_T$  in the East vs the West. Another  
591 explanation might be that SFE and FluxCom both have the highest performance (for  
592 both low  $\sigma_\varepsilon$  and high  $R_T$ ) in shrublands and grassland land cover types, both of which  
593 are often found in the Western US (Dewitz, 2024). This finding is in contrast to Zhu et al.  
594 (2024), who found that daily and monthly SFE had the lowest correlation and highest  
595 root mean squared error at the eight towers in shrublands, relative to towers in other  
596 land covers.

597

### 598 **4.3. The benefits and limitations of triple collocation**

599 Triple collocation makes several assumptions, including that the random errors between  
600 the datasets are independent, that the random errors are stationary across time, and  
601 that the random errors can be described linearly. The assumptions of triple collocation  
602 are also implicitly made by more standard validation analyses such as comparison via

603 RMSE (Gruber et al., 2016). However, these assumptions are expected to be violated to  
604 some degree, regardless of how carefully comparison datasets are chosen. One reason  
605 for this is that most ET models contain at least some overlapping input data, for  
606 example the commonly used MODIS reflectance products for vegetation, such as leaf  
607 area index, are used as inputs to FLUXCOM, ERA5-Land, and GLEAM (ECMWF, 2018;  
608 Jung et al., 2019; Miralles et al., 2025). Any overlap in model input data reduces the  
609 likelihood that the resulting ET estimates will have independent errors. Triple collocation  
610 may also fail or wrongly estimate dataset errors if random error magnitudes vary in time  
611 or are not well described linearly. Therefore, it is not uncommon for triple collocation  
612 studies to have invalid pixel results (e.g. He et al., 2023). Some triple collocation studies  
613 also choose to pre-filter pixels to ensure high correlation coefficient between the raw  
614 datasets (Gruber et al., 2016; McColl et al., 2014), which also leads to pixels where  
615 triple collocation results are missing.

616         One way to increase the confidence in an application of triple collocation is to  
617 repeat the analysis for multiple triplets, as performed here. Violations in the triple  
618 collocation assumptions would lead to differences in the estimated error statistic for a  
619 given dataset depending on which datasets are used for comparison (He et al., 2023;  
620 McColl et al., 2014). We found that invalid triple collocation results were more prevalent  
621 when FluxCom and ERA5-Land were compared within the same triplet, regardless of  
622 the third dataset. This suggests that the assumption of independent errors may be  
623 worse between these two datasets, despite their seemingly larger input difference than  
624 GLEAM and FluxCom, for example, which both incorporate machine learning.  
625 Nevertheless, the overall high agreement between different triple collocation estimates  
626 for the other triplets - and the lack of coherent spatial pattern in error variability across  
627 triplets (Figure 5) - strongly increases our confidence that our overall error estimates are  
628 robust.

629         One limitation of triple collocation is that it cannot provide information about  
630 multiplicative dataset biases ( $\beta$ ) beyond estimating relative biases with reference to one  
631 member of each triplet which is assumed to have no bias (Gruber et al., 2016; McColl et  
632 al., 2014). However, previous work suggests that SFE may have issues with bias  
633 particularly along aridity gradients. For example, Chen et al. (2021) and Zhu et al.  
634 (2024) both found that SFE ET had higher bias in arid conditions and tended to  
635 underestimate ET in wet conditions. This same pattern was also observed for  
636 comparisons of in situ SFE to eddy covariance data (McColl and Rigden, 2020; Thakur  
637 et al., 2025). While we do not consider bias because triple collocation only allows for its  
638 calculation relative to a comparison dataset, we do see that SFE  $\sigma_\epsilon$  is highest at the  
639 driest and wettest pixels compared to pixels with intermediate mean annual  
640 precipitation. SFE  $R_T$ , on the other hand, shows only a weak but slightly decreasing  
641 relationship with increasing mean annual precipitation. Further in situ validation of SFE

642 in the wettest and driest ecosystems would be beneficial. However the problem of ET  
643 overestimation in arid conditions - when surface evaporation is high in general - is not  
644 unique to SFE (McColl and Rigden, 2020; Miralles et al., 2016; Salvucci and Gentine,  
645 2013). Despite the assumptions and limitations of triple collocation, the method's ability  
646 to quantify error statistics relative to true ET without needing an error-free dataset of ET  
647 remains a substantial and unique benefit.

648

## 649 **5. Conclusions**

650 SFE allows for observational, data-driven estimates of ET with no tunable parameters or  
651 land surface information required. That SFE estimates ET from atmospheric conditions  
652 alone has several advantages: It can be calculated at a variety of scales and  
653 geographic domains and it provides an opportunity to test hypotheses about vegetation  
654 response to environmental drivers without assuming that response a priori in the  
655 creation of the ET estimate itself. The lack of parameterization for SFE eases issues of  
656 circularity constraining research into essential outstanding challenges in ecohydrology,  
657 such as the response of ET to drought (Zhao et al., 2022) and the inference of  
658 subsurface water storage from changes in vegetation behavior (Dralle et al., 2020;  
659 Feldman et al., 2023; Stocker et al., 2023). Based on triple collocation - and despite its  
660 simplicity - SFE exhibits comparable performance to the more complex ET estimates  
661 from GLEAM, FluxCom, and ERA5-Land.

662

## 663 **6. Code availability**

664 Code is available on GitHub at

665 [https://github.com/erica-mccormick/sfe\\_et\\_and\\_triple\\_collocation](https://github.com/erica-mccormick/sfe_et_and_triple_collocation).

666

## 667 **7. Data availability**

668 All of the data used to estimate SFE ET as well as the comparison ET datasets are  
669 publicly available online. Daily 4 km estimates of SFE ET across CONUS from 1979 to  
670 2025 are available on Zenodo at <https://zenodo.org/records/17903676>. DOI:  
671 10.5281/zenodo.17903676.

672

## 673 **8. Acknowledgments**

674 ELM, LES, and AGK were supported by NSF DEB 1942133. AGK was also supported  
675 by the Alfred P. Sloan Foundation and by the Gordon and Betty Moore Foundation  
676 under grant 11974. ELM was supported by the Stanford University Diversifying  
677 Academia Recruiting Excellence Doctoral Fellowship and by the NSF GRFP. KAM

678 acknowledges funding from NSF grant AGS-2129576, an NSF CAREER award  
679 (AGS-2441565), and a Sloan Research Fellowship (FG-2023-19963).

680

## 681 **9. Competing interests**

682 The authors declare that they have no conflict of interest.

683

## 684 **10. References**

685

686 Abatzoglou, J. T.: Development of gridded surface meteorological data for ecological  
687 applications and modelling, *Int. J. Climatol.*, 33, 121–131,  
688 <https://doi.org/10.1002/joc.3413>, 2013.

689 ArcGIS Data and Maps: USA Detailed Water Bodies, 2023. Beven, K. J. and Kirkby, M.  
690 J.: A physically-based, variable contributing area model of basin hydrology, *Hydrol. Sci.*  
691 *Bull.*, 24, 43–69, <https://doi.org/10.1080/02626667909491834>, 1979.

692 Burnett, M. W., Quetin, G. R., and Konings, A. G.: Data-driven estimates of  
693 evapotranspiration and its controls in the Congo Basin, *Hydrol. Earth Syst. Sci.*, 24,  
694 4189–4211, <https://doi.org/10.5194/hess-24-4189-2020>, 2020.

695 Chen, F., Crow, W. T., Bindlish, R., Colliander, A., Burgin, M. S., Asanuma, J., and Aida,  
696 K.: Global-scale evaluation of SMAP, SMOS and ASCAT soil moisture products using  
697 triple collocation, *Remote Sens. Environ.*, 214, 1–13,  
698 <https://doi.org/10.1016/j.rse.2018.05.008>, 2018.

699 Chen, S., McColl, K. A., Berg, A., and Huang, Y.: Surface Flux Equilibrium Estimates of  
700 Evapotranspiration at Large Spatial Scales, *J. Hydrometeorol.*, 22, 765–779,  
701 <https://doi.org/10.1175/JHM-D-20-0204.1>, 2021.

702 Clothier, B. E., Clawson, K. L., Pinter Jr, P. J., Moran, M. S., Reginato, R. J., & Jackson,  
703 R. D. (1986). Estimation of soil heat flux from net radiation during the growth of alfalfa.  
704 *Agricultural and forest meteorology*, 37(4), 319-329.

705 Crow, W. T., Lei, F., Hain, C., Anderson, M. C., Scott, R. L., Billesbach, D., and  
706 Arkebauer, T.: Robust estimates of soil moisture and latent heat flux coupling strength  
707 obtained from triple collocation: ESTIMATION OF LAND COUPLING STRENGTH,  
708 *Geophys. Res. Lett.*, 42, 8415–8423, <https://doi.org/10.1002/2015GL065929>, 2015.

709 Dewitz: National Land Cover Database (NLCD) 2019 Products (ver. 3.0, February  
710 2024), <https://doi.org/10.5066/P9KZCM54>, 2024.

711 Doelling, D. R., Loeb, N. G., Keyes, D. F., Nordeen, M. L., Morstad, D., Nguyen, C.,  
712 Wielicki, B. A., Young, D. F., and Sun, M.: Geostationary Enhanced Temporal

713 Interpolation for CERES Flux Products, *J. Atmospheric Ocean. Technol.*, 30,  
714 1072–1090, <https://doi.org/10.1175/JTECH-D-12-00136.1>, 2013.

715 Dralle, D. N., Hahm, W. J., Chadwick, K. D., McCormick, E. L., and Rempe, D. M.:  
716 Technical note: Accounting for snow in the estimation of root-zone water storage  
717 capacity from precipitation and evapotranspiration fluxes, *Hydrol. Earth Syst. Sci.*, 1–9,  
718 <https://doi.org/10.5194/hess-2020-602>, 2020.

719 Draper, C., Reichle, R., De Jeu, R., Naeimi, V., Parinussa, R., and Wagner, W.:  
720 Estimating root mean square errors in remotely sensed soil moisture over continental  
721 scale domains, *Remote Sens. Environ.*, 137, 288–298,  
722 <https://doi.org/10.1016/j.rse.2013.06.013>, 2013.

723 ECMWF: IFS Documentation CY45R1 - Part IV: Physical processes,  
724 <https://doi.org/10.21957/4WHWO8JW0>, 2018.

725 Entekhabi, D., Reichle, R. H., Koster, R. D., and Crow, W. T.: Performance Metrics for  
726 Soil Moisture Retrievals and Application Requirements, *J. Hydrometeorol.*, 11, 832–840,  
727 <https://doi.org/10.1175/2010JHM1223.1>, 2010.

728 Eyring, V., Bony, S., Meehl, G. A., Senior, C. A., Stevens, B., Stouffer, R. J., and Taylor,  
729 K. E.: Overview of the Coupled Model Intercomparison Project Phase 6 (CMIP6)  
730 experimental design and organization, *Geosci. Model Dev.*, 9, 1937–1958,  
731 <https://doi.org/10.5194/gmd-9-1937-2016>, 2016.

732 Feldman, A. F., Short Gianotti, D. J., Dong, J., Akbar, R., Crow, W. T., McColl, K. A.,  
733 Konings, A. G., Nippert, J. B., Tumber-Dávila, S. J., Holbrook, N. M., Rockwell, F. E.,  
734 Scott, R. L., Reichle, R. H., Chatterjee, A., Joiner, J., Poulter, B., and Entekhabi, D.:  
735 Remotely Sensed Soil Moisture Can Capture Dynamics Relevant to Plant Water  
736 Uptake, *Water Resour. Res.*, 59, e2022WR033814,  
737 <https://doi.org/10.1029/2022WR033814>, 2023.

738 Ferreira, V. G., Montecino, H. D. C., Yakubu, C. I., and Heck, B.: Uncertainties of the  
739 Gravity Recovery and Climate Experiment time-variable gravity-field solutions based on  
740 three- cornered hat method, *J. Appl. Remote Sens.*, 10, 015015,  
741 <https://doi.org/10.1117/1.JRS.10.015015>, 2016.

742 Fisher, J. B., Lee, B., Purdy, A. J., Halverson, G. H., Dohlen, M. B., Cawse-Nicholson,  
743 K., Wang, A., Anderson, R. G., Aragon, B., Arain, M. A., Baldocchi, D. D., Baker, J. M.,  
744 Barral, H., Bernacchi, C. J., Bernhofer, C., Biraud, S. C., Bohrer, G., Brunzell, N.,  
745 Cappelaere, B., Castro- Contreras, S., Chun, J., Conrad, B. J., Cremonese, E.,  
746 Demarty, J., Desai, A. R., De Ligne, A., Foltýnová, L., Goulden, M. L., Griffis, T. J.,  
747 Grünwald, T., Johnson, M. S., Kang, M., Kelbe, D., Kowalska, N., Lim, J., Mainassara,

748 I., McCabe, M. F., Missik, J. E. C., Mohanty, B. P., Moore, C. E., Morillas, L., Morrison,  
749 R., Munger, J. W., Posse, G., Richardson, A. D., Russell, E. S., Ryu, Y.,  
750 Sanchez-Azofeifa, A., Schmidt, M., Schwartz, E., Sharp, I., Šigut, L., Tang, Y., Hulley,  
751 G., Anderson, M., Hain, C., French, A., Wood, E., and Hook, S.: ECOSTRESS: NASA's  
752 Next Generation Mission to Measure Evapotranspiration From the International Space  
753 Station, *Water Resour. Res.*, 56, e2019WR026058,  
754 <https://doi.org/10.1029/2019WR026058>, 2020.

755 Friedlingstein, P., Jones, M. W., O'Sullivan, M., Andrew, R. M., Hauck, J., Peters, G. P.,  
756 Peters, W., Pongratz, J., Sitch, S., Le Quéré, C., Bakker, D. C. E., Canadell, J. G., Ciais,  
757 P., Jackson, R. B., Anthoni, P., Barbero, L., Bastos, A., Bastrikov, V., Becker, M., Bopp,  
758 L., Buitenhuis, E., Chandra, N., Chevallier, F., Chini, L. P., Currie, K. I., Feely, R. A.,  
759 Gehlen, M., Gilfillan, D., Gkritzalis, T., Goll, D. S., Gruber, N., Gutekunst, S., Harris, I.,  
760 Haverd, V., Houghton, R. A., Hurtt, G., Ilyina, T., Jain, A. K., Joetzjer, E., Kaplan, J. O.,  
761 Kato, E., Klein Goldewijk, K., Korsbakken, J. I., Landschützer, P., Lauvset, S. K.,  
762 Lefèvre, N., Lenton, A., Lienert, S., Lombardozzi, D., Marland, G., McGuire, P. C.,  
763 Melton, J. R., Metz, N., Munro, D. R., Nabel, J. E. M. S., Nakaoka, S.-I., Neill, C., Omar,  
764 A. M., Ono, T., Pregon, A., Pierrot, D., Poulter, B., Rehder, G., Resplandy, L.,  
765 Robertson, E., Rödenbeck, C., Séférian, R., Schwinger, J., Smith, N., Tans, P. P., Tian,  
766 H., Tilbrook, B., Tubiello, F. N., van der Werf, G. R., Wiltshire, A. J., and Zaehle, S.:  
767 Global Carbon Budget 2019, *Earth Syst. Sci. Data*, 11, 1783–1838,  
768 <https://doi.org/10.5194/essd-11-1783-2019>, 2019.

769 Good, S. P., Noone, D., and Bowen, G.: Hydrologic connectivity constrains partitioning  
770 of global terrestrial water fluxes, *Science*, 349, 175–177,  
771 <https://doi.org/10.1126/science.aaa5931>, 2015.

772 Green, J. K., Konings, A. G., Alemohammad, S. H., Berry, J., Entekhabi, D., Kolassa, J.,  
773 Lee, J.-E., and Gentile, P.: Regionally strong feedbacks between the atmosphere and  
774 terrestrial biosphere, *Nat. Geosci.*, 10, 410–414, <https://doi.org/10.1038/ngeo2957>,  
775 2017.

776 Gruber, A., Su, C.-H., Zwieback, S., Crow, W., Dorigo, W., and Wagner, W.: Recent  
777 advances in (soil moisture) triple collocation analysis, *Int. J. Appl. Earth Obs.*  
778 *Geoinformation*, 45, 200–211, <https://doi.org/10.1016/j.jag.2015.09.002>, 2016.

779 He, Y., Wang, C., Hu, J., Mao, H., Duan, Z., Qu, C., Li, R., Wang, M., and Song, X.:  
780 Discovering Optimal Triplets for Assessing the Uncertainties of Satellite-Derived  
781 Evapotranspiration Products, *Remote Sens.*, 15, 3215,  
782 <https://doi.org/10.3390/rs15133215>, 2023.

783 Hersbach, H., Bell, B., Berrisford, P., Hirahara, S., Horányi, A., Muñoz-Sabater, J.,  
784 Nicolas, J., Peubey, C., Radu, R., Schepers, D., Simmons, A., Soci, C., Abdalla, S.,

785 Abellan, X., Balsamo, G., Bechtold, P., Biavati, G., Bidlot, J., Bonavita, M., De Chiara,  
786 G., Dahlgren, P., Dee, D., Diamantakis, M., Dragani, R., Flemming, J., Forbes, R.,  
787 Fuentes, M., Geer, A., Haimberger, L., Healy, S., Hogan, R. J., Hólm, E., Janisková, M.,  
788 Keeley, S., Laloyaux, P., Lopez, P., Lupu, C., Radnoti, G., De Rosnay, P., Rozum, I.,  
789 Vamborg, F., Villaume, S., and Thépaut, J.: The ERA5 global reanalysis, *Q. J. R.*  
790 *Meteorol. Soc.*, 146, 1999–2049, <https://doi.org/10.1002/qj.3803>, 2020.

791 Jung, M., Koirala, S., Weber, U., Ichii, K., Gans, F., Camps-Valls, G., Papale, D.,  
792 Schwalm, C., Tramontana, G., and Reichstein, M.: The FLUXCOM ensemble of global  
793 land-atmosphere energy fluxes, *Sci. Data*, 6, 74,  
794 <https://doi.org/10.1038/s41597-019-0076-8>, 2019.

795 Koppa, A., Rains, D., Hulsman, P., Poyatos, R., and Miralles, D. G.: A deep  
796 learning-based hybrid model of global terrestrial evaporation, *Nat. Commun.*, 13, 1912,  
797 <https://doi.org/10.1038/s41467-022-29543-7>, 2022.

798 Martens, B., Miralles, D. G., Lievens, H., Van Der Schalie, R., De Jeu, R. A. M.,  
799 Fernández-Prieto, D., Beck, H. E., Dorigo, W. A., and Verhoest, N. E. C.: GLEAM v3:  
800 satellite-based land evaporation and root-zone soil moisture, *Geosci. Model Dev.*, 10,  
801 1903–1925, <https://doi.org/10.5194/gmd-10-1903-2017>, 2017.

802 Martens, B., Schumacher, D. L., Wouters, H., Muñoz-Sabater, J., Verhoest, N. E. C.,  
803 and Miralles, D. G.: Evaluating the land-surface energy partitioning in ERA5, *Geosci.*  
804 *Model Dev.*, 13, 4159–4181, <https://doi.org/10.5194/gmd-13-4159-2020>, 2020.

805 McColl, K. A. and Rigden, A. J.: Emergent Simplicity of Continental Evapotranspiration,  
806 *Geophys. Res. Lett.*, 47, <https://doi.org/10.1029/2020GL087101>, 2020.

807 McColl, K. A., Vogelzang, J., Konings, A. G., Entekhabi, D., Piles, M., and Stoffelen, A.:  
808 Extended triple collocation: Estimating errors and correlation coefficients with respect to  
809 an unknown target, *Geophys. Res. Lett.*, 41, 6229–6236,  
810 <https://doi.org/10.1002/2014GL061322>, 2014.

811 McColl, K. A., Salvucci, G. D., and Gentine, P.: Surface Flux Equilibrium Theory  
812 Explains an Empirical Estimate of Water-Limited Daily Evapotranspiration, *J. Adv.*  
813 *Model. Earth Syst.*, 11, 2036–2049, <https://doi.org/10.1029/2019MS001685>, 2019.

814 Mesinger, F., DiMego, G., Kalnay, E., Mitchell, K., Shafran, P. C., Ebisuzaki, W., Jović,  
815 D., Woollen, J., Rogers, E., Berbery, E. H., Ek, M. B., Fan, Y., Grumbine, R., Higgins,  
816 W., Li, H., Lin, Y., Manikin, G., Parrish, D., and Shi, W.: North American Regional  
817 Reanalysis, *Bull. Am. Meteorol. Soc.*, 87, 343–360,  
818 <https://doi.org/10.1175/BAMS-87-3-343>, 2006.

819 Miralles, D. G., Crow, W. T., and Cosh, M. H.: Estimating Spatial Sampling Errors in  
820 Coarse-Scale Soil Moisture Estimates Derived from Point-Scale Observations, *J.*  
821 *Hydrometeorol.*, 11, 1423–1429, <https://doi.org/10.1175/2010JHM1285.1>, 2010.

822 Miralles, D. G., Holmes, T. R. H., De Jeu, R. A. M., Gash, J. H., Meesters, A. G. C. A.,  
823 and Dolman, A. J.: Global land-surface evaporation estimated from satellite-based  
824 observations, *Hydrol. Earth Syst. Sci.*, 15, 453–469,  
825 <https://doi.org/10.5194/hess-15-453-2011>, 2011.

826 Miralles, D. G., Jiménez, C., Jung, M., Michel, D., Ershadi, A., McCabe, M. F., Hirschi,  
827 M., Martens, B., Dolman, A. J., Fisher, J. B., Mu, Q., Seneviratne, S. I., Wood, E. F., and  
828 Fernández-Prieto, D.: The WACMOS-ET project – Part 2: Evaluation of global terrestrial  
829 evaporation data sets, *Hydrol. Earth Syst. Sci.*, 20, 823–842,  
830 <https://doi.org/10.5194/hess-741-20-823-2016>, 2016.

831 Miralles, D. G., Bonte, O., Koppa, A., Baez-Villanueva, O. M., Tronquo, E., Zhong, F.,  
832 Beck, H. E., Hulsman, P., Dorigo, W., Verhoest, N. E. C., and Haghdoost, S.: GLEAM4:  
833 global land evaporation and soil moisture dataset at 0.1° resolution from 1980 to near  
834 present, *Sci. Data*, 12, 416, <https://doi.org/10.1038/s41597-025-04610-y>, 2025.

835 Mu, Q., Zhao, M., and Running, S. W.: Improvements to a MODIS global terrestrial  
836 evapotranspiration algorithm, *Remote Sens. Environ.*, 115, 1781–1800,  
837 <https://doi.org/10.1016/j.rse.2011.02.019>, 2011.

838 Muñoz-Sabater, J., Dutra, E., Agustí-Panareda, A., Albergel, C., Arduini, G., Balsamo,  
839 G., Boussetta, S., Choulga, M., Harrigan, S., Hersbach, H., Martens, B., Miralles, D. G.,  
840 Piles, M., Rodríguez-Fernández, N. J., Zsoter, E., Buontempo, C., and Thépaut, J.-N.:  
841 ERA5-Land: a state-of-the-art global reanalysis dataset for land applications, *Earth*  
842 *Syst. Sci. Data*, 13, 4349–4383, <https://doi.org/10.5194/essd-13-4349-2021>, 2021.

843 Oki, T. and Kanae, S.: Global Hydrological Cycles and World Water Resources, *Freshw.*  
844 *Resour.*, 313, 5, 2006.

845 Salvucci, G. D. and Gentile, P.: Emergent relation between surface vapor conductance  
846 and relative humidity profiles yields evaporation rates from weather data, *Proc. Natl.*  
847 *Acad. Sci.*, <https://doi.org/10.1073/pnas.1215844110>, 2013.

848 Santanello Jr, J. A., & Friedl, M. A. (2003). Diurnal covariation in soil heat flux and net  
849 radiation. *Journal of Applied Meteorology*, 42(6), 851-862.

850 Savoca, M. E., Senay, G. B., Maupin, M. A., Kenny, J. F., and Perry, C. A.: Actual  
851 evapotranspiration modeling using the operational Simplified Surface Energy Balance  
852 (SSEBop) approach, Reston, VA, <https://doi.org/10.3133/sir20135126>, 2013.

853 Scipal, K., Holmes, T., De Jeu, R., Naeimi, V., and Wagner, W.: A possible solution for  
854 the problem of estimating the error structure of global soil moisture data sets, *Geophys.*  
855 *Res. Lett.*, 35, <https://doi.org/10.1029/2008gl035599>, 2008.

856 Stocker, B. D., Tumber-Dávila, S. J., Konings, A. G., Anderson, M. C., Hain, C., and  
857 Jackson, R. B.: Global patterns of water storage in the rooting zones of vegetation, *Nat.*  
858 *Geosci.*, 16, 250–256, <https://doi.org/10.1038/s41561-023-01125-2>, 2023.

859 Stoffelen, A.: Toward the true near-surface wind speed: Error modeling and calibration  
860 using triple collocation, *J. Geophys. Res. Oceans*, 103, 7755–7766,  
861 <https://doi.org/10.1029/97JC03180>, 1998.

862 Su, C. H., Ryu, D., Crow, W. T., & Western, A. W. (2014). Beyond triple collocation:  
863 Applications to soil moisture monitoring. *Journal of Geophysical Research:*  
864 *Atmospheres*, 119(11), 6419-6439.

865 Sun, J., McColl, K. A., Wang, Y., Rigden, A. J., Lu, H., Yang, K., Li, Y., and Santanello,  
866 J. A.: Global evaluation of terrestrial near-surface air temperature and specific humidity  
867 retrievals from the Atmospheric Infrared Sounder (AIRS), *Remote Sens. Environ.*, 252,  
868 112146, <https://doi.org/10.1016/j.rse.2020.112146>, 2021.

869 Teuling, A. J., Seneviratne, S. I., Stöckli, R., Reichstein, M., Moors, E., Ciais, P.,  
870 Luyssaert, S., Van Den Hurk, B., Ammann, C., Bernhofer, C., Dellwik, E., Gianelle, D.,  
871 Gielen, B., Grünwald, T., Klumpp, K., Montagnani, L., Moureaux, C., Sottocornola, M.,  
872 and Wohlfahrt, G.: Contrasting response of European forest and grassland energy  
873 exchange to heatwaves, *Nat. Geosci.*, 3, 722–727, <https://doi.org/10.1038/ngeo950>,  
874 2010.

875 Thakur, H., Raghav, P., Kumar, M., and Wolkeba, F.: Surface Flux Equilibrium  
876 Theory-Derived Evapotranspiration Estimate Outperforms ECOSTRESS, MODIS, and  
877 SSEBop Products, *Geophys. Res. Lett.*, 52, e2025GL114822,  
878 <https://doi.org/10.1029/2025GL114822>, 2025.

879 United States Census Bureau: TIGER/Line Shapefile, 2019, nation, U.S., Coastline  
880 National Shapefile, 2019.

881 Xia, Y., Mitchell, K., Ek, M., Sheffield, J., Cosgrove, B., Wood, E., Luo, L., Alonge, C.,  
882 Wei, H., Meng, J., Livneh, B., Lettenmaier, D., Koren, V., Duan, Q., Mo, K., Fan, Y., and  
883 Mocko, D.: Continental-scale water and energy flux analysis and validation for the North  
884 American Land Data Assimilation System project phase 2 (NLDAS-2): 1.  
885 Intercomparison and application of model products, *J. Geophys. Res. Atmospheres*,  
886 117, 2011JD016048, <https://doi.org/10.1029/2011JD016048>, 2012.

887 Yamazaki, D., Ikeshima, D., Sosa, J., Bates, P. D., Allen, G. H., and Pavelsky, T. M.:  
888 MERIT Hydro: A High-Resolution Global Hydrography Map Based on Latest  
889 Topography Dataset, *Water Resour. Res.*, 55, 5053–5073,  
890 <https://doi.org/10.1029/2019WR024873>, 2019.

891 Yang, Y., Roderick, M. L., Guo, H., Miralles, D. G., Zhang, L., Fatichi, S., Luo, X., Zhang,  
892 Y., McVicar, T. R., Tu, Z., Keenan, T. F., Fisher, J. B., Gan, R., Zhang, X., Piao, S.,  
893 Zhang, B., and Yang, D.: Evapotranspiration on a greening Earth, *Nat. Rev. Earth*  
894 *Environ.*, 4, 626–641, <https://doi.org/10.1038/s43017-023-00464-3>, 2023.

895 Yilmaz, M. T. and Crow, W. T.: Evaluation of Assumptions in Soil Moisture Triple  
896 Collocation Analysis, *J. Hydrometeorol.*, 15, 1293–1302,  
897 <https://doi.org/10.1175/JHM-D-13-0158.1>, 2014.

898 Yin, X., Jiang, B., Liang, S., Li, S., Zhao, X., Wang, Q., Xu, J., Han, J., Liang, H., Zhang,  
899 X., Liu, Q., Yao, Y., Jia, K., and Xie, X.: Significant discrepancies of land surface daily  
900 net radiation among ten remotely sensed and reanalysis products, *Int. J. Digit. Earth*,  
901 16, 3725–3752, <https://doi.org/10.1080/17538947.2023.2253211>, 2023.

902 Zhao, M., A. G., Liu, Y., and Konings, A. G.: Evapotranspiration frequently increases  
903 during droughts, *Nat. Clim. Change*, 12, 1024–1030,  
904 <https://doi.org/10.1038/s41558-022-01505-3>, 807 2022.

905 Zhu, W., Yu, X., Wei, J., and Lv, A.: Surface flux equilibrium estimates of evaporative  
906 fraction and evapotranspiration at global scale: Accuracy evaluation and performance  
907 comparison, *Agric. Water Manag.*, 291, 108609,  
908 <https://doi.org/10.1016/j.agwat.2023.108609>, 2024.

909